ACADEMIC PRESS

Available online at www.sciencedirect.com

SCIENCE DIRECT®

Journal of Computational Physics 186 (2003) 503–526

JOURNAL OF COMPUTATIONAL PHYSICS

www.elsevier.com/locate/jcp

Unsteady free surface flow simulation over complex topography with a multidimensional upwind technique

P. Brufau *, P. García-Navarro

Fluid Mechanics, C.P.S., University of Zaragoza (Spain), María de Luna 3, 50015 Zaragoza, Spain

Received 2 May 2001; received in revised form 8 May 2002; accepted 7 November 2002

Abstract

In the context of numerical techniques for solving unsteady free surface problems, finite element and finite volume approximations are widely used. A class of upwind methods which attempts to model the equations in a genuinely multidimensional manner has been recently introduced as an alternative. Multidimensional upwind schemes (MUS) were developed initially for the approximation of steady-state solutions of the two-dimensional Euler equations on unstructured grids, although they can be applicable to any system of hyperbolic conservation laws, such as the shallow water equations. The formal analogy between the two systems of equations is useful for simple cases. However, in practical applications of interest in hydraulics, complex geometries and bottom slope variation can lead to important numerical errors produced by an inadequate source term discretization. This problem has been analyzed and, in this work, the necessity of a multidimensional upwind discretization of the source terms is justified. The basis of the numerical method is stated and the particular adaptation to unsteady shallow water flows over irregular geometry is described. As test cases, laboratory experimental data are used together with academic tests for validation.

Keywords: Multidimensional upwind; Shallow water; Unsteady flow; Source terms

1. Introduction

A perfect scheme for the solution of multidimensional non-linear systems of partial differential equations governing fluid motion has not yet been found, despite years of research effort and many scientific contributions. Upwind methods are very popular in the modelling of advection dominated flows and in particular those which contain strong discontinuities. The essence of the upwind method depends on the reduction of the problem to a set of subproblems that are (almost) independent. The best solution

* Corresponding author.
E-mail addresses: brufau@posta.unizar.es (P. Brufau), pigar@posta.unizar.es (P. García-Navarro).

0021-9991/03/$ - see front matter
doi:10.1016/S0021-9991(03)00072-X

techniques for these scalar subproblems can then be studied [21]. These methods are frequently extended to solve systems of equations in higher dimensions.

Initial attempts to extend 1D upwind techniques to higher dimensions were all based on 1D upwind concepts applied within a dimensional splitting framework, and modelling the flow by solving simple Riemann problems across cell interfaces on structured grids. The next step consisted of applying the same idea on unstructured grids using the projection of the problem onto the normal to the edge directions. Unstructured grids have many advantages for multidimensional flow analysis, particularly their flexibility when constructing boundary fitted grids for complex geometries, and their general lack of preferential grid directions. Even so, locally, schemes based on structured/unstructured grids are the same when the numerical flux normal to the cell face is only evaluated in the 1D manner. The result is a solution algorithm which depends on geometrical variables which have little or no relation with the relevant flow directions. In particular, cell boundaries are used to define a 1D direction along which the upwinding takes place.

Some authors considered that it was necessary to incorporate genuinely multidimensional physics into these algorithms. The first step was taken by Davis [5] who suggested that the shock capturing capabilities of upwind methods could be improved by rotating the Riemann problem to align it with the direction of physically important flow gradients. Variables like flow direction or velocity gradient direction over a cell face are taken into account for the discretization. This work was extended by Levy et al. [22] and Tamura and Fujii [32]. An alternative method was developed independently by Rumsey et al. [30] and Parpia and Michalek [25]. Common to these methods is the fact that the multispatial physics is added at the cell interfaces, thus retaining some 1D aspects.

The methods which use a genuinely multidimensional physical model for the upwinding do not fit in a standard finite volume approach where the representation of the unknowns is considered to be only piecewise continuous. In this respect they are much closer to finite element methods based on linear elements, with which they share a continuous piecewise linear representation over the cells. On the other hand, they share with upwind methods the properties of asymmetric upwinded stencils and control of monotonicity across discontinuities, and they can be considered as truly multidimensional generalizations of the TVD upwind methods [7]. These schemes are designed to monitor the average space variation of the approximation to the solution within a complete grid cell rather than concentrating on the activity at the interfaces.

The basis of the multidimensional upwinding techniques (MUS) applied in this work for 2D shallow water flows [11] is the assumption that any observed gradients in the initial data at the start of a time step are linked to the presence of simple waves in the flow. Since an infinite number of simple wave patterns could be responsible for the same observed gradients, it is necessary to hypothesize the number and nature of the waves present and this is known as a wave model [8]. Simple wave models have been used in the work presented for their conceptual simplicity although they are not much used nowadays. Their main disadvantage is that they can introduce unnecessary numerical dissipation. It is important that the orientation of the waves should not be constrained by the directions of the grid. Roe developed a number of wave models based on simple waves [26]. Rudgyard constructed other simple wave models [29]. We have selected Rudgyard's wave model as the most adequate for our interests due to the robustness it offers [13]. Deconinck et al. [6] devised an alternative strategy for decomposing the fluctuation, based on an attempt to diagonalize the system of equations. More recent developments have involved the diagonalization of a preconditioned set of equations and result in a maximally decoupled system [10]. A preconditioned wave model of this type [17] has proved to be the best of the current decompositions for steady problems [16] but, in contrast to simple wave models, seems unlikely to provide a simple extension to unsteady flows. The next step is to update the solution in a way that acknowledges the direction of propagation of each wave in the model using appropriate advection schemes: N, NN, PSI among others for steady-state problems. The PSI scheme (positive streamwise invariant) satisfies all of the desired properties and is the scheme adopted here for the distribution of fluctuations. A good reference can be found in [9]. None of these schemes developed

originally is higher than first order accurate in space for time-dependent problems. This problem has recently been addressed successfully by equating the PSI scheme with a mass lumped finite element scheme, the constructing an appropriate mass matrix [24,33] to give the corresponding full finite element method [23] or by combining the PSI and Lax-Wendroff schemes in a manner similar to flux-corrected transport.

The basic theory was developed for homogeneous systems of equations. Some mathematical models for fluid problems require the presence of source terms, as for instance in the shallow water system of equations to consider bottom variations and friction losses. The discretization of the source terms can be done following a pointwise approach. A multidimensional upwind approach is adopted here for the discretization of bed slope terms in order to ensure an exact balance between bed slope and pressure terms in zero-velocity flow. The idea follows from previous works developed using finite volume based upwind schemes [12,18,34]. It will be shown in the applications that this upwinding reproduces exactly steady state of still water. Unsteady problems have only really been studied in depth more recently, and then mainly in the scalar case [17], but some test cases presented here in which validation with experimental data is carried out will show a next step of this work. Unsteady shallow water flow over irregular bed introduces a new difficulty: the wetting–drying front. The front represents a moving boundary always involving inclined partially wetted cells whose numerical treatment is crucial for the overall performance of the numerical scheme. If these cells are discretized as ordinary cells, the wetting front is observed to advance flooding upper areas that should remain dry. In Section 5 the strategy to correct this tendency will be detailed.

2. Numerical technique

The steps to follow for constructing a wave model based MUS for a non-linear system of equations are the following.

Step A: Construct a suitable scheme for the solution of the scalar advection equation. This involves the development of "fluctuation distribution" techniques in two dimensions. They use a piecewise continuous linear data representation and involve the calculation of the fluctuation (or residual) within each cell and its distribution in an upwind manner to update the flow variables at the vertices.

Step B: Identify the element propagation properties and directions within each cell. This requires the development of a wave decomposition model which splits the fluctuations into components, each of which corresponds to a simple wave solution of the equations. The system of equations requires a linearization and the fluctuations due to each scalar wave can then be distributed using an advection scheme (PSI) from step A.

It must be remarked that step B is only necessary for systems of equations and the linearization for non-linear problems.

2.1. Scalar case

Before attempting to model the full two-dimensional shallow water system of equations it is necessary to consider the numerical solution of a linear scalar equation like

$$\frac{\partial w}{\partial t} + \mathbf{a} \cdot \nabla w = 0, \quad \mathbf{a} = (a_x, a_y), \tag{1}$$

where $\mathbf{a}$ is a constant vector. We will assume that the given physical domain is discretized using triangular cells and a set of initial solution values w_i stored at the nodes of the mesh. For each cell T a fluctuation is defined as

$$\phi_T = \int_T \frac{\partial w}{\partial t}\, \mathrm{d}S = -\int_T \mathbf{a} \cdot \nabla w \, \mathrm{d}S \tag{2}$$

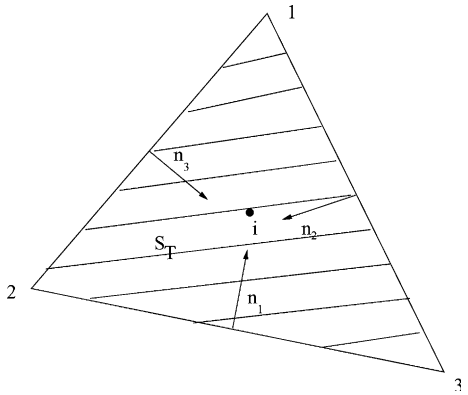

Fig. 1. Details of the normals at the edges of a cell.

and a cell residual R_T as

$$R_T = -\frac{1}{S_T}\phi_T = \frac{1}{S_T}\int_T \mathbf{a}\cdot\nabla w\,\mathrm{d}S = -\frac{1}{S_T}\oint_C w\mathbf{a}\cdot\mathbf{n}\,\mathrm{d}C, \tag{3}$$

where C represents the cell boundary and $\mathbf{n}$ the inward normal to that boundary (see Fig. 1). In (3), Gauss theorem and the constancy of $\mathbf{a}$ have been used. ϕ_T or equivalently R_T, contains information on the state of the cell. The changes made to the values of the w_i's in T over a time step will be proportional to ϕ_T (or R_T). The distribution of the information to the nodes must be done in a way which ensures conservation [33].

From the properties of the normals in the cell and the additional assumption that the solution varies linearly within each element, it is possible [9] to identify a discrete approximation of ∇w,

$$\nabla w_T = \frac{1}{2S_T}\sum_{i=1}^{3} w_i\mathbf{n}_i. \tag{4}$$

Then

$$R_T = \frac{1}{S_T}\int_T \mathbf{a}\cdot\nabla w\,\mathrm{d}S = \frac{1}{S_T}\mathbf{a}\cdot\nabla w_T\int_T \mathrm{d}S = \mathbf{a}\cdot\nabla w_T \tag{5}$$

or equivalently

$$R_T = \frac{1}{S_T}\sum_{i=1}^{3} w_i k_i, \quad \phi_T = -\sum_{i=1}^{3} w_i k_i, \tag{6}$$

which introduces the quantities

$$k_i = \frac{1}{2}\mathbf{a}\cdot\mathbf{n}_i \tag{7}$$

containing information about the direction of the advection speed relative to the cell edges. k_i can be used to decide whether flow enters or leaves the triangle through a particular edge and, in that sense, are a useful tool for imposing the upwind properties of the technique [15].

Residuals and fluctuations are cell-based quantities and are used for constructing the updating of the nodal solution values. For this purpose, coefficients D_T^i, defining the weightings which determine the distribution of the residual to the nodes of the cell, are introduced. They must satisfy in every cell

$$\sum_{i=1}^{3} D_T^i = 1 \tag{8}$$

for conservation and consistency of the scheme. By using a simple forward Euler time differencing the following procedure can be defined to update the variables at all the nodes

$$w_i^{n+1} = w_i^n - \frac{\Delta t}{S_i}\left(\sum_{T_i} S_T D_T^i R_T^n\right) \tag{9}$$

in which T_i indicates a sum over all the cells meeting at node i, and where $S_i = \frac{1}{3}\sum_{T_i} S_T$ is the area of the median dual cell around node i, one-third the total area of the triangles having i as vertex.

There exist many criteria for the design of advection schemes according to the choice of the distribution coefficients D_T^i. The most commonly used non-linear scheme, even for linear equations, is the PSI scheme [10] which is based on the linear, positive N scheme [15]. Since the advection schemes are not problem dependent, we will not go into more details about their particular construction and description. We refer to very good reviews made in [15] and [33].

2.2. Non-linear systems of equations

When the equation itself is non-linear a suitable linearization must be performed and then the technique described for a linear equation applied. Moreover, the application of multidimensional upwinding to a general non-linear 2D system of conservation laws

$$\frac{\partial \mathbf{W}}{\partial t} + \nabla \cdot \mathbf{F}(\mathbf{W}) = 0, \quad \mathbf{F} = (\mathbf{f}, \mathbf{g}) \tag{10}$$

in which $\mathbf{W}$ represents the vector of conserved variables and $\mathbf{f}, \mathbf{g}$ the fluxes in the coordinate directions, requires a discrete form of the quasi-linear system

$$\frac{\partial \mathbf{W}}{\partial t} + (\mathbf{A}, \mathbf{B}) \cdot \nabla \mathbf{W} = 0, \quad \mathbf{A} = \mathbf{f}_{\mathbf{W}}, \quad \mathbf{B} = \mathbf{g}_{\mathbf{W}}. \tag{11}$$

In the conservative formulation, the fluctuation is defined as

$$\phi_T = \int_T \frac{\partial \mathbf{W}}{\partial t}\,\mathrm{d}S = -\int_T (\mathbf{f}_x + \mathbf{g}_y)\,\mathrm{d}S = -\int_T (\mathbf{A}\mathbf{W}_x + \mathbf{B}\mathbf{W}_y)\,\mathrm{d}S. \tag{12}$$

Following step B, a linearization and wave decomposition model is necessary to split the residual into components, each of which will be distributed with an advection scheme to know the new value of the flow variables at the vertices.

2.2.1. Linearization and wave models

The system of equations requires a linearization before going on with the development of the wave model. For convenience, in this case, we consider a linearized system of equations written in other variables $\mathbf{V}$ which will be named as "*primitive variables*".

$$\frac{\partial \mathbf{V}}{\partial t} + (\mathbf{E}, \mathbf{H}) \cdot \nabla \mathbf{V} = 0. \tag{13}$$

If $\mathbf{M}$ is the matrix which gives the transformation of conserved variables $\mathbf{W}$ to primitive variables $\mathbf{V}$,

$$\mathbf{M} = \frac{\partial \mathbf{W}}{\partial \mathbf{V}}, \tag{14}$$

the matrices $\mathbf{E}$ and $\mathbf{H}$ are defined as

$$\mathbf{E} = \mathbf{M}^{-1}\mathbf{A}\mathbf{M}, \quad \mathbf{H} = \mathbf{M}^{-1}\mathbf{B}\mathbf{M}. \tag{15}$$

A simple wave solution can be found, according to Roe [26,27] in the form

$$\mathbf{V} = \mathbf{V}(\xi) \quad \text{with } \xi = \mathbf{x}\cdot\mathbf{n}_\theta - \lambda_\theta t, \tag{16}$$

where $\mathbf{n}_\theta = (\cos\theta, \sin\theta)$ gives the direction of propagation and λ_θ the speed of the particular wave. If we note that

$$\frac{\partial \mathbf{V}}{\partial t} = -\lambda_\theta \frac{\mathrm{d}\mathbf{V}}{\mathrm{d}\xi} \tag{17}$$

and

$$\nabla \mathbf{V} = \frac{\mathrm{d}\mathbf{V}}{\mathrm{d}\xi}\mathbf{n}_\theta, \tag{18}$$

from (13) it follows that

$$-\lambda_\theta \frac{\mathrm{d}\mathbf{V}}{\mathrm{d}\xi} + (\mathbf{E}\cos\theta + \mathbf{H}\sin\theta)\frac{\mathrm{d}\mathbf{V}}{\mathrm{d}\xi} = 0, \tag{19}$$

which means that $\mathrm{d}\mathbf{V}/\mathrm{d}\xi$ are the right eigenvectors of the matrix

$$\mathbf{M}^* = \mathbf{E}\cos\theta + \mathbf{H}\sin\theta \tag{20}$$

and λ_θ the corresponding eigenvalues.

It is possible then to express the gradient as a sum

$$\frac{\partial \mathbf{V}_i}{\partial x_j} = \sum_{k=1}^{N_\mathrm{w}} (\alpha \mathbf{r}_i \mathbf{n}_j)^k \tag{21}$$

or

$$\nabla \mathbf{V} = \sum_{k=1}^{N_\mathrm{w}} (\alpha \mathbf{r} \otimes \mathbf{n})^k, \quad \mathbf{n}^k = (\cos\theta^k, \sin\theta^k) \tag{22}$$

in which N_w is the number of waves in the decomposition or, equivalently

$$\begin{aligned} \mathbf{V}_x &= \sum_{k=1}^{N_\mathrm{w}} \alpha^k \mathbf{r}^k \cos\theta^k, \\ \mathbf{V}_y &= \sum_{k=1}^{N_\mathrm{w}} \alpha^k \mathbf{r}^k \sin\theta^k. \end{aligned} \tag{23}$$

The vectors $\mathbf{r}^k$ are right eigenvectors of the matrix $\mathbf{M}^*$. The variables α^k represent weighting coefficients of the sum and θ^k are the different angles of each wave.

This is a general form of wave decomposition model in which the gradient of the variables has been expressed as a sum of waves with different angles of propagation. Arriving to that point, an advection scheme can be used to distribute the waves to the vertices as it was done in (9) for the scalar case.

In order to make the method rely on the set of primitive variables, the relation between the two sets of variables can be used [13]. Provided that the primitive variables $\mathbf{V}$ are linear over the cells T, the gradients $\nabla\mathbf{V}$ are constant, and this enables us to write the fluctuation (12) as

$$\boldsymbol{\phi}_T = -(\tilde{\mathbf{S}}\mathbf{V}_x + \tilde{\mathbf{T}}\mathbf{V}_y)S_T \tag{24}$$

with

$$\tilde{\mathbf{S}} = \mathbf{S}(\tilde{\mathbf{V}}), \quad \tilde{\mathbf{T}} = \mathbf{T}(\tilde{\mathbf{V}}). \tag{25}$$

Definition of $\tilde{\mathbf{V}}$, $\tilde{\mathbf{S}}$ and $\tilde{\mathbf{T}}$ for the shallow water system of equations can be found in [33,34]. It will be split into simple waves and then re-expressed in terms of the conserved variables. This will be illustrated in next section.

3. Application to the non-linear shallow water system of equations

The homogeneous version of the shallow water hyperbolic non-linear system of equations in terms of the conserved variables (h depth of water, hu and hv unit discharges along the coordinate directions, u and v being the depth averaged velocity components)

$$\mathbf{W} = (h, hu, hv)^{\mathrm{T}} \tag{26}$$

is [11]

$$\frac{\partial \mathbf{W}}{\partial t} + \nabla \cdot \mathbf{F}(\mathbf{W}) = 0, \quad \mathbf{F} = (\mathbf{f}, \mathbf{g}), \tag{27}$$

where the fluxes are

$$\mathbf{f} = \left(hu, hu^2 + g\frac{h^2}{2}, huv\right)^{\mathrm{T}}, \quad \mathbf{g} = \left(hv, huv, hv^2 + g\frac{h^2}{2}\right)^{\mathrm{T}}. \tag{28}$$

Rewritten in the quasi-linear form (11), the two Jacobian matrices are

$$\mathbf{A} = \mathbf{f}_{\mathbf{W}} = \begin{pmatrix} 0 & 1 & 0 \\ u^2 + gh & 2u & 0 \\ uv & v & u \end{pmatrix}, \quad \mathbf{B} = \mathbf{g}_{\mathbf{W}} = \begin{pmatrix} 0 & 0 & 1 \\ uv & v & u \\ v^2 + gh & 0 & 2v \end{pmatrix}. \tag{29}$$

As stated in Section 2.2, a non-linear system of equations needs a linearization in terms of primitive variables. In the shallow water case, these are defined as

$$\mathbf{V} = (h, u, v)^{\mathrm{T}} \tag{30}$$

and the shallow water model in the non-conservative formulation (13) introduces the new matrices

$$\mathbf{E} = \begin{pmatrix} u & h & 0 \\ g & 2u & 0 \\ 0 & 0 & u \end{pmatrix}, \quad \mathbf{H} = \begin{pmatrix} v & 0 & h \\ 0 & v & 0 \\ g & 0 & 2v \end{pmatrix}. \tag{31}$$

The matrix $\mathbf{M}$ has the form

$$\mathbf{M} = \frac{\partial \mathbf{W}}{\partial \mathbf{V}} = \begin{pmatrix} 1 & 0 & 0 \\ u & h & 0 \\ v & 0 & h \end{pmatrix} \tag{32}$$

and the averaged variables are defined simply by

$$\tilde{\mathbf{V}} = \begin{pmatrix} \tilde{h} \\ \tilde{u} \\ \tilde{v} \end{pmatrix} = \frac{1}{3} \begin{pmatrix} h_1 + h_2 + h_3 \\ u_1 + u_2 + u_3 \\ v_1 + v_2 + v_3 \end{pmatrix}, \tag{33}$$

summing over the nodal values at the vertices of the triangle T.

We can rewrite the fluctuation in terms of suitable averages of the conservative variables

$$\boldsymbol{\phi}_T = -S_T(\tilde{\mathbf{f}}_x + \tilde{\mathbf{g}}_y) = -(\tilde{\mathbf{S}}\mathbf{M}^{-1}(\tilde{\mathbf{V}})\tilde{\mathbf{W}}_x + \tilde{\mathbf{T}}\mathbf{M}^{-1}(\tilde{\mathbf{V}})\tilde{\mathbf{W}}_y)S_T = -(\tilde{\mathbf{A}}\tilde{\mathbf{W}}_x + \tilde{\mathbf{B}}\tilde{\mathbf{W}}_y)S_T, \tag{34}$$

which allows, finally, the identifications of $\tilde{\mathbf{A}}$ and $\tilde{\mathbf{B}}$ in terms of $\tilde{\mathbf{V}}$:

$$\begin{aligned} \tilde{\mathbf{A}} &= \mathbf{S}(\tilde{\mathbf{V}})\mathbf{M}^{-1}(\tilde{\mathbf{V}}) = \left.\frac{\partial \mathbf{f}}{\partial \mathbf{V}}\right|_{\tilde{\mathbf{V}}} \left.\frac{\partial \mathbf{V}}{\partial \mathbf{W}}\right|_{\tilde{\mathbf{V}}} = \left.\frac{\partial \mathbf{f}}{\partial \mathbf{W}}\right|_{\tilde{\mathbf{V}}} = \mathbf{A}(\tilde{\mathbf{V}}), \\ \tilde{\mathbf{B}} &= \mathbf{T}(\tilde{\mathbf{V}})\mathbf{M}^{-1}(\tilde{\mathbf{V}}) = \left.\frac{\partial \mathbf{g}}{\partial \mathbf{V}}\right|_{\tilde{\mathbf{V}}} \left.\frac{\partial \mathbf{V}}{\partial \mathbf{W}}\right|_{\tilde{\mathbf{V}}} = \left.\frac{\partial \mathbf{g}}{\partial \mathbf{W}}\right|_{\tilde{\mathbf{V}}} = \mathbf{B}(\tilde{\mathbf{V}}). \end{aligned} \tag{35}$$

Eq. (33) together with the expressions of the matrices $\tilde{\mathbf{S}}, \tilde{\mathbf{T}}$ (35) can reconstruct Eq. (24). Here, only approximations of $\tilde{\mathbf{A}}$ and $\tilde{\mathbf{B}}$ are given because exact evaluation of the integrals is not possible. The linearization used is not conservative, although there exists a conservative formulation for $\tilde{\mathbf{V}}$ [28] but it is considerably more complicated.

Recalling that what we usually have at the beginning of the time step are the values of the conserved variables at the vertices of the triangular mesh, the steps to follow are: compute the primitive variables $\mathbf{V}$ from the known $\mathbf{W}$, work out the gradients $\nabla\mathbf{V} = (\mathbf{V}_x, \mathbf{V}_y)$ within each triangle, and decompose the residual into parts that can be explained as due to the passage of a simple wave. The next thing we have to do is to compute the residuals $\mathbf{R}_T$ or the fluctuations and distribute them to the vertices of every cell by means of an advection scheme.

3.1. Wave model for the shallow water equations

The $\sim$ symbol, indicating a linearized quantity, has been excluded from now on for clarity. In 2D shallow water flows, matrices $\mathbf{A}$ and $\mathbf{B}$ cannot generally be diagonalized simultaneously (hence the difficulty in constructing suitable wave models). Instead, an approximate diagonalization can be constructed via a 3-parameter similarity transformation [13]. This method has an advantage over the existing simple wave models in having the correct number of components for linearity preservation but the propagation directions, which depend on the parameters which define the similarity transformation, are usually chosen to depend on the solution gradients, creating problems with convergence to a steady state so they are not used in this work.

In Section 2.2.1, we found that the gradient can be expressed as a sum

$$\nabla\mathbf{V} = \sum_{k=1}^{N_w} \alpha^k \mathbf{r}^k \otimes \mathbf{n}^k, \quad \mathbf{n}^k = (\cos\theta^k, \sin\theta^k) \tag{36}$$

in which N_w is the number of waves in the decomposition. In the 2D shallow water case, it represents a system of six equations, where we have two spatial derivatives for each of the three variables. Therefore, it allows for six unknowns. These must correspond to coefficients or angles of propagation of suitable choices of waves whose advection will represent the total fluctuation.

The vectors $\mathbf{r}^k$, right eigenvectors of the matrix $\mathbf{M}^*$ defined in (20), take one of the three forms (representing two types of gravity wave and a shear wave) in the shallow water case

$$\mathbf{r}^1 = \begin{pmatrix} 1 \\ \frac{g}{c}\cos\theta \\ \frac{g}{c}\sin\theta \end{pmatrix}, \quad \mathbf{r}^2 = \begin{pmatrix} 1 \\ -\frac{g}{c}\cos\theta \\ -\frac{g}{c}\sin\theta \end{pmatrix}, \quad \mathbf{r}^3 = \begin{pmatrix} 0 \\ -\sin\theta \\ \cos\theta \end{pmatrix}. \tag{37}$$

The equivalent of the speed of sound in gas-dynamics is the velocity of small perturbations in still water, and is given by $c = \sqrt{gh}$.

The connection between the gradient of the primitive variables and that of the averaged conservative variables can be used to develop the latter as

$$\begin{aligned} \mathbf{W}_x &= \sum_{k=1}^{N_w} \alpha^k \mathbf{r}_c^k \cos\theta^k, \\ \mathbf{W}_y &= \sum_{k=1}^{N_w} \alpha^k \mathbf{r}_c^k \sin\theta^k, \end{aligned} \tag{38}$$

where now, $\mathbf{r}_c^k$ represent the right eigenvectors of the matrix

$$\mathbf{M}_c^* = \mathbf{A}\cos\,\theta + \mathbf{B}\sin\,\theta \tag{39}$$

and can be worked out through $\mathbf{r}_c^k = \mathbf{M}(\mathbf{V})\mathbf{r}^k$. It is worth noting here that the subscript c represents a quantity associated with the conservative equations and the two matrices $\mathbf{M}^*$ and $\mathbf{M}_c^*$ share the same set of eigenvalues (or wave speeds), λ^k, given by

$$\begin{aligned} \lambda^1 &= u\cos\theta + v\sin\theta + c, \\ \lambda^2 &= u\cos\theta + v\sin\theta - c, \\ \lambda^3 &= u\cos\theta + v\sin\theta. \end{aligned} \tag{40}$$

The residual, following (34), then can be split in a sum of waves

$$\begin{aligned} \mathbf{R}_T = -\frac{1}{S_T}\boldsymbol{\phi}_T &= \mathbf{A}\sum_{k=1}^{N_w} \alpha^k \mathbf{r}_c^k \cos\theta^k + \mathbf{B}\sum_{k=1}^{N_w} \alpha^k \mathbf{r}_c^k \sin\theta^k = \sum_{k=1}^{N_w} \alpha^k \left(\mathbf{A}\cos\theta^k + \mathbf{B}\sin\theta^k\right)\mathbf{r}_c^k = \sum_{k=1}^{N_w} \alpha^k \lambda^k \mathbf{r}_c^k \\ &= \sum_{k=1}^{N_w} (\boldsymbol{\lambda}^k \cdot \nabla \mathbf{X}^k)\mathbf{r}_c^k \end{aligned} \tag{41}$$

for appropriate choices of the wave velocities $\boldsymbol{\lambda}^k$ and "characteristic" gradients $\nabla\mathbf{X}^k$. This is simply a sum of components of precisely the form seen in (5).

Rudgyard's wave model, used in this work for simplicity, is mainly based on the idea [29] of obtaining six waves by choosing two, in principle, arbitrary propagation angles, θ_1 and θ_2, and performing a decomposition of the gradient

$$\nabla\mathbf{V} = \sum_{k=1}^{3} \alpha_{\theta_1}^k \mathbf{r}_{\theta_1}^k \otimes \mathbf{n}_{\theta_1} + \sum_{k=1}^{3} \alpha_{\theta_2}^k \mathbf{r}_{\theta_2}^k \otimes \mathbf{n}_{\theta_2}, \tag{42}$$

which contains six free parameters, the six coefficients α. The vectors $\mathbf{n}_\theta = (\cos\theta, \sin\theta)$ are again the unit vectors in the directions θ, and $\mathbf{r}_\theta^k$ are the right eigenvectors of the matrix $\mathbf{M}^*$, a full set of eigenvectors as defined in (37) for each value of θ. In order to solve for the unknowns, use is also made of the left eigenvectors of that matrix

$$\mathbf{l}_\theta^1 = \begin{pmatrix} \frac{1}{2} \\ \frac{c}{2g}\cos\theta \\ \frac{c}{2g}\sin\theta \end{pmatrix}, \quad \mathbf{l}_\theta^2 = \begin{pmatrix} \frac{1}{2} \\ -\frac{c}{2g}\cos\theta \\ -\frac{c}{2g}\sin\theta \end{pmatrix}, \quad \mathbf{l}_\theta^3 = \begin{pmatrix} 0 \\ -\sin\theta \\ \cos\theta \end{pmatrix}, \tag{43}$$

and of the unit vector normal to $\mathbf{n}_\theta$,

$$\mathbf{s}_\theta = (-\sin\theta, \cos\theta). \tag{44}$$

Multiplication of (42) on the left by $\mathbf{l}_{\theta_1}^1$ and the left projection over $\mathbf{s}_{\theta_2}$ give

$$\mathbf{s}_{\theta_2} \cdot \left(\mathbf{l}_{\theta_1}^1 \cdot \nabla \mathbf{V}\right) = \alpha_{\theta_1}^1 (\mathbf{s}_{\theta_2} \cdot \mathbf{n}_{\theta_1}), \tag{45}$$

where the property $\mathbf{l}_\theta^i \cdot \mathbf{r}_\theta^j = \delta_{ij}$ and the orthogonality between vectors $\mathbf{s}$ and $\mathbf{n}$ have been used.

From (45), we obtain

$$\alpha_{\theta 1}^k = -\frac{\mathbf{s}_{\theta 2} \cdot \left(\mathbf{l}_{\theta 1}^k \cdot \nabla \mathbf{V}\right)}{\sin(\theta_2 - \theta_1)}, \quad \alpha_{\theta 2}^k = \frac{\mathbf{s}_{\theta 1} \cdot \left(\mathbf{l}_{\theta 2}^k \cdot \nabla \mathbf{V}\right)}{\sin(\theta_2 - \theta_1)}. \tag{46}$$

In this case, the associated advection velocities in (41) are chosen so that, from (46), $\nabla \mathbf{X}^k = \mathbf{l}_\theta^k \cdot \nabla \mathbf{V}$.

The angles are chosen from one option proposed by Rudgyard [29], in which the equation

$$\mathbf{u} \cdot \mathbf{n} - c = 0 \tag{47}$$

must be satisfied. From algebraic manipulation, the expression for the angles becomes

$$\theta^1 = \arctan\left(\frac{v + u\sqrt{Fr^2 - 1}}{u - v\sqrt{Fr^2 - 1}}\right), \quad \theta^2 = \arctan\left(\frac{v - u\sqrt{Fr^2 - 1}}{u + v\sqrt{Fr^2 - 1}}\right), \tag{48}$$

Fr being the Froude number.

The PSI advection scheme is used now for the distribution of each wave to the nodes constituting the cell. The residual can be distributed to the nodes of a cell in many ways. However, when treating an advection equation it can be argued to use the physical propagation direction for distributing the residual. For the PSI scheme, the idea is to enforce invariance along streamlines (characteristics). This is obtained by updating the nodes of the triangle so that a correspondence is established between the points that share a streamline, which is equivalent to requiring $\mathbf{R}_T^{n+1} = 0$. Inflow and outflow sides are considered in the cells and in order to satisfy invariance along streamlines, the value of the variables at the downstream node must be changed. The details can be found in [9,15].

The nodal updating follows the form

$$S_i \mathbf{W}_i^{n+1} = S_i \mathbf{W}_i^n - \Delta t \sum_{T_i} S_T D_T^i \mathbf{R}_T^n, \tag{49}$$

S_i being the area of the dual cell around node i and D_T^i representing the cumulative effect of the coefficients used for each individual wave in the decomposition of the residual (41) to the nodes of a cell. The residual $\mathbf{R}_T$ is computed in all the cells and the variables stored at each node i are updated summing over all the cells meeting at node i.

Boundary cells are computed as ordinary cells, so that all their nodes are updated using inside information. The updating of boundary nodes in boundary cells is completed with information from the physical boundary conditions.

4. Source terms

The presence of important source terms in the equation may destroy positivity and hence robustness of the numerical scheme. This is the reason why we have maintained Rudgyard's simple wave model for a shallow water flow because source terms can be dominant and this wave model is more robust than others.

Once a multidimensional upwind technique has been described to discretize the homogeneous shallow water system of equations, we are going to analyze what happens if source terms are present in the equations

$$\frac{\partial \mathbf{W}}{\partial t} + \nabla \cdot \mathbf{F}(\mathbf{W}) = \mathbf{Z}(x, \mathbf{W}), \tag{50}$$

allowing for instance the modelling of flow over a varying bed topography.

Two approaches have been used in the past [11,16]; pointwise and averaging, which lead to numerical errors. Hence, a better approach is proposed here that guarantees at least one steady state. Both flux and bottom slope are expressed in the equations by spatial derivatives which suggests that the discretization must be equal to ensure the conservation property at steady state, following previous work [34]. Numerical results showing the errors produced with a pointwise approach are shown in Section 6.

Source terms within the basic shallow water model can be divided in two types: bed slope ($\mathbf{Z}^1$) and friction ($\mathbf{Z}^2$) terms

$$\mathbf{Z} = \mathbf{Z}^1 + \mathbf{Z}^2 \tag{51}$$

being

$$\mathbf{Z}^1 = \begin{pmatrix} 0 \\ -gh\frac{\partial z_b}{\partial x} \\ -gh\frac{\partial z_b}{\partial y} \end{pmatrix}, \quad \mathbf{Z}^2 = \begin{pmatrix} 0 \\ -ghS_{fx} \\ -ghS_{fy} \end{pmatrix}. \tag{52}$$

z_b is the bed level taken from an arbitrary horizontal reference. S_{fx}, S_{fy} are friction losses that can be expressed in terms of Manning's roughness coefficient [4]; the latter do not involve spatial derivatives and, in general, a pointwise discretization is used for this term.

The multidimensional upwind approach presented here is based on the introduction of bottom variations in the definition of the fluctuation/residual as it was done with the fluxes, looking for the equilibrium between fluxes and bed slope source terms to achieve exactly steady state. The cell residual is redefined as

$$\mathbf{R}_T = \frac{1}{S_T} \int_T \left[(\mathbf{A}, \mathbf{B}) \cdot \nabla \mathbf{W} - \mathbf{Z}^1 \right] \mathrm{d}S \tag{53}$$

in such a way that the updating of variables is extended from (49) to

$$S_i \mathbf{W}_i^{n+1} = S_i \mathbf{W}_i^n - \Delta t \sum_{T_i} S_T D_T^i \mathbf{R}_T^n + \Delta t \left(\mathbf{Z}_T^2 \right)^n. \tag{54}$$

The residual $\mathbf{R}_T$, now containing fluxes and bed variations, is computed in all the cells and the variables stored at each node i are updated, summing over all the cells meeting at node i. D_T^i is not simply a coefficient but represents the cumulative effect of the coefficients used for each individual wave in the decomposition of the residual in (41). Friction terms $\mathbf{Z}^2$ are incorporated in a pointwise cell averaged form.

As stated before, in the particular case of the shallow water system, it is convenient to express the equations in terms of primitive variables $\mathbf{V}$ in a non-conservative formulation to exploit the hypothesis of linear representation of $\mathbf{V}$ in each cell.

In terms of primitive variables $\mathbf{V}$,

$$\frac{\partial \mathbf{V}}{\partial t} + (\mathbf{E}, \mathbf{H}) \cdot \nabla \mathbf{V} - \hat{\mathbf{Z}}^1 = \hat{\mathbf{Z}}^2, \tag{55}$$

$\hat{\mathbf{Z}}^{1,2}$ being the source terms associated to the primitive variables $\mathbf{V}$. In Section 2.2.1, the expression of the gradient of primitive variables as a sum of waves (22)

$$\nabla \mathbf{V} = \sum_{k=1}^{3} \alpha_{\theta_1}^k \mathbf{r}_{\theta_1}^k \otimes \mathbf{n}_{\theta_1}^k + \sum_{k=1}^{3} \alpha_{\theta_2}^k \mathbf{r}_{\theta_2}^k \otimes \mathbf{n}_{\theta_2}^k \tag{56}$$

was used as the basis of the method.

The bed slope source term includes the gradient of the bottom levels and, in that sense, can be regarded as the gradient of another variable z_b. We have stated that the gradient of primitive variables $\nabla \mathbf{V}$ is decomposed in simple waves which splits the fluctuation into components. Now, the bottom variations are included in the definition of the fluctuation, indicating that this term must be decomposed in the same wave model used for the gradient $\nabla \mathbf{V}$. Then, we can write

$$\nabla \mathbf{V} - \hat{\mathbf{Z}}^1 = \sum_{k=1}^{3} \left(\alpha_{\theta_1}^k \mathbf{r}_{\theta_1}^k - \boldsymbol{\beta}_{\theta_1}^k \right) \otimes \mathbf{n}_{\theta_1} + \sum_{k=1}^{3} \left(\alpha_{\theta_2}^k \mathbf{r}_{\theta_2}^k - \boldsymbol{\beta}_{\theta_2}^k \right) \otimes \mathbf{n}_{\theta_2} \tag{57}$$

using Rudgyard's wave model. For dimensional purposes

$$\hat{\mathbf{Z}}^1 = \tilde{\mathbf{Z}}^1 \otimes \mathbf{n}, \tag{58}$$

because

$$\nabla \mathbf{V} = \frac{\partial \mathbf{V}_i}{\partial x_j} = \begin{pmatrix} \partial \mathbf{V}_1/\partial x & \partial \mathbf{V}_1/\partial y \\ \partial \mathbf{V}_2/\partial x & \partial \mathbf{V}_2/\partial y \\ \partial \mathbf{V}_3/\partial x & \partial \mathbf{V}_3/\partial y \end{pmatrix} \tag{59}$$

and

$$\hat{\mathbf{Z}}^1 = \tilde{\mathbf{Z}}^1 \otimes \mathbf{n} = \tilde{\mathbf{Z}}_i^1 n_j = \begin{pmatrix} \tilde{\mathbf{Z}}_1^1 n_1 & \tilde{\mathbf{Z}}_1^1 n_2 \\ \tilde{\mathbf{Z}}_2^1 n_1 & \tilde{\mathbf{Z}}_2^1 n_2 \\ \tilde{\mathbf{Z}}_3^1 n_1 & \tilde{\mathbf{Z}}_3^1 n_2 \end{pmatrix}, \tag{60}$$

which decomposes bottom variations in x, y directions. $\boldsymbol{\beta}_\theta^k$ are the weighting coefficients of the decomposition. C-property of Vázquez–Cendón [34] must be satisfied so that the numerical scheme does not perturb a still water steady initial state, i.e., the discretization cannot create spurious unsteady effects. What must be enforced is the balance between the fluxes and the source terms discretizations. For a multidimensional upwind scheme in an initially steady state this property implies

$$\frac{\partial \mathbf{W}}{\partial t} = 0 \Rightarrow \mathbf{R}_T = 0. \tag{61}$$

This condition gives different weighting coefficients of the bed variation decomposition depending on the wave model used. In our case, the simple wave model leads to

$$\mathbf{R}_T = \sum_{k=1}^{N_w} \left(\lambda^k \alpha^k \mathbf{r}_c^k - \boldsymbol{\beta}^k \right) = 0. \tag{62}$$

With some algebraic manipulations it is easy to verify that (62) with Rudgyard's wave model is satisfied only if $\boldsymbol{\beta}_{\theta_1}, \boldsymbol{\beta}_{\theta_2}$ are expressed in the form

$$\hat{\boldsymbol{\beta}}^k_{\theta_1} = -\frac{\mathbf{s}_{\theta_2} \cdot (\mathbf{l}^k_{\theta_1} \otimes \tilde{\mathbf{Z}}^1)}{\sin(\theta_2 - \theta_1)}, \quad \hat{\boldsymbol{\beta}}^k_{\theta_2} = -\frac{\mathbf{s}_{\theta_1} \cdot (\mathbf{l}^k_{\theta_2} \otimes \tilde{\mathbf{Z}}^1)}{\sin(\theta_2 - \theta_1)} \tag{63}$$

with

$$\tilde{\mathbf{Z}}^1 = -g \begin{pmatrix} 0 \\ \partial z_b/\partial x \\ \partial z_b/\partial y \end{pmatrix}. \tag{64}$$

5. Wetting–drying fronts

The procedure described in Sections 3 and 4 is applied for the ordinary nodes and cells, that is, those representing points at the interior of the wetted domain. The boundaries of the wetted domain are defined by the nodes not completely surrounded by other wet cells. All these nodes actually require the definition of suitable boundary conditions in order to reach the solution of a problem. However, for transient flows a distinction can be made considering either wetted domains fixed in extension, that is, limited by vertical walls, or those whose size changes as time progresses, that is, those involving sloping walls and moving boundaries.

Boundary conditions are applied only at fixed boundaries. The moving boundaries are considered in our work as wetting fronts and included in the ordinary procedure through a calculation that assumes zero water depth for the dry nodes. This approach provides satisfactory results when dealing with wetting fronts over flat or downward sloping surfaces but often meets with difficulties in the presence of adverse slopes. In general, numerical techniques adapted to cope with zero depth nodes are unable to solve correctly situations of still water in a partially wet domain of irregular shape, generating spurious velocities in the wet/dry contour and often violating mass conservation. This is precisely the result of our experience with the multidimensional upwind method presented in this paper. Even though the incorporation of the bed slope terms into the multidimensional upwinding solved some of the numerical errors present in simulations over variable bed slope, it was clear that something else had to be done in the presence of partially wet bed slopes.

Previous works on this topic can be found. Some authors working with finite elements solve the problem allowing the controlled use of negative depths [14,19,20]. In finite volume methods a Riemann problem is solved across each cell edge so, in an attempt to generate a simple and efficient rule within this framework some authors [1,31] propose a solid wall treatment at the wetting–drying fronts. This option does not prove optimal and, instead, an alternative was adapted in [3]. Following this last work, the wetting–drying technique has been adapted to multidimensional upwind techniques taking into account both the similarities and differences between upwinding in the context of finite volumes and multidimensional upwinding. In a finite element philosophy, the MUS works on a local basis, that is, it considers gradients and propagations into a single cell, achieving in this way a global effect. According to this, a simple procedure has been designed. For the sake of simplicity in the discussion, let us consider a case of still water ($u = v = 0$). With reference to Fig. 2, we assume that the wetting/drying frontier can occur inside a cell in the two situations sketched in the figure among other possibilities: either one node is dry and two are wet

$$h_1 = 0, \quad h_2 > 0, \quad h_3 > 0 \tag{65}$$

with

$$d_1 > d_2 \quad \text{and} \quad d_1 > d_3, \quad d = h + z_b, \tag{66}$$

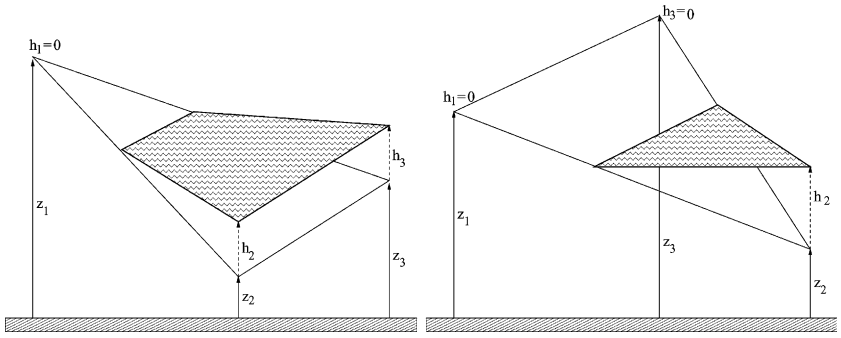

Fig. 2. Two different wetting–drying situations in a cell.

or two are dry and one is wet

$$h_1 = 0, \quad h_2 > 0, \quad h_3 = 0 \tag{67}$$

with

$$d_1 > d_2 \quad \text{and} \quad d_3 > d_2. \tag{68}$$

It can be seen from (62) that the discretization of the mass equation to ensure quiescent flow at each cell (flux and source discretizations must balance) leads to the equilibrium condition

$$\nabla d = 0 \Rightarrow \nabla z_b = -\nabla h. \tag{69}$$

Condition (69) is not always fulfilled due to the discrete representation of the variables and can be demonstrated using the analytical expressions of h and z_b at the wetting–drying front. The steady flow problem is hence converted into an unsteady one producing movement in water that should be always at steady state, and mass conservation is lost. In order to avoid the numerical error, the technique proposed here is to enforce the local redefinition of the bottom level gradient at the wetting–drying cell to fulfill the equilibrium condition (69) and therefore mass conservation. In such cases, as shown in Fig. 3, the gradient of the bottom level is redefined enforcing

$$\nabla z_b = -\nabla h. \tag{70}$$

In Fig. 3 the representation of one of these situations can be observed. In case (66) occurs in a cell (Fig. 3 top right), the linear representation of the variables within a cell in the discrete model is unable to reproduce the real situation shown on the top left. Instead, it gives non-horizontal water surface incompatible with zero velocity steady flow. The idea of the proposed wetting–drying condition (70) consists of modifying locally the bottom level of the dry node (Fig. 3, bottom left) so that a horizontal water level is achieved on the cell. Now, the representation of the model (Fig. 3, bottom right), being linear, gives the same original discrete water volume, horizontal surface, zero velocity and mass conservation is guaranteed in each cell at least at this steady state.

In unsteady cases, i.e., for wetting fronts advancing over an adverse dry slope, the procedure followed is the same. However in this case the numerical representation of the slope in a cell may produce a too fast propagation of the front. It is necessary to reduce to zero the velocity components u, v of the dry nodes; otherwise some water could easily jump to the dry node.

For practical implementation, we have selected 10^{-10} as the threshold that defines a dry node. The results show sensitivity to the choice of this value.

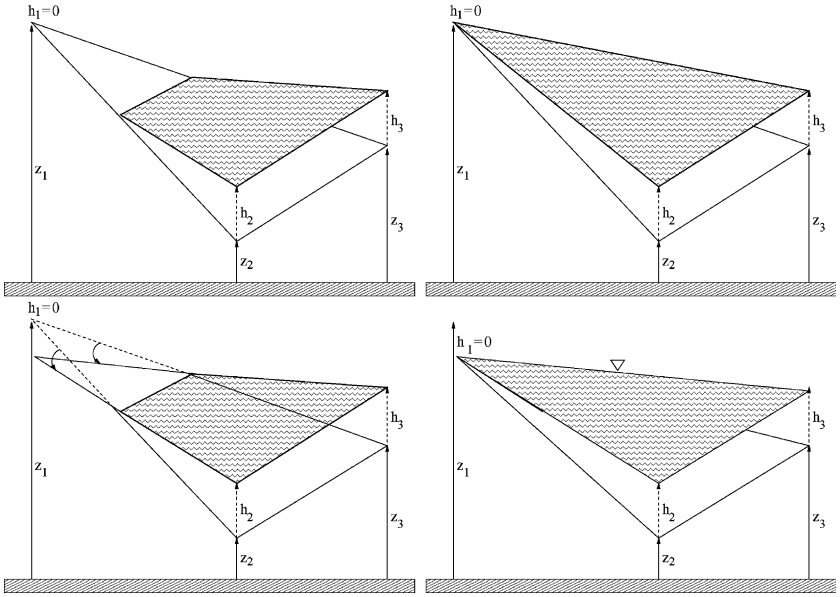

Fig. 3. Geometrical interpretation of the wetting–drying condition, model representation (right), real situation (left). The bed redefinition technique is illustrated in the lower pictures.

6. Numerical results

6.1. Steady flow over a bump

The first test is the simulation of steady flow over a bump to demonstrate the necessity of applying MUS to bottom variations. This is an academic test and the numerical experiment consists of a square pool 1 m × 1 m. At the center of the pool a symmetric bump is situated, mathematically defined by

$$z_b(x,y) = \max\left[0, 0.25 - 5\left(\left(x-\frac{1}{2}\right)^2 + \left(y-\frac{1}{2}\right)^2\right)\right]. \tag{71}$$

Fig. 4 represents the geometry of the problem. On the left we can see the iso-contour levels of the bottom and on the right a 3D plot of the numerical experiment. Two initial conditions are going to be analyzed with initial water level covering totally or partially the bump and we are interested in the ability of the numerical method to maintain steady state. Initial conditions covering totally the bump are

$$d = h + z_b = 0.5 \text{ m}, \quad u = 0 \text{ m/s}, \quad v = 0 \text{ m/s}. \tag{72}$$

This is an ideal case with no friction and the pool is totally closed by solid vertical walls. The flow evolves during 1 min and steady state must be preserved. A comparison of the numerical results using a pointwise approach (a,b) or an upwind approach (c,d) in terms of iso-contours and velocity field (a,c) and free surface plot (b,d) is shown in Fig. 5. Both numerical calculations have been carried out using the same triangular mesh with 1600 cells. If the bed slope discretization is correct, no change in free surface or velocity field (nil in this case) can be observed because no external influence is present and equilibrium must be conserved. In Fig. 5 it is obvious that steady state is maintained with a MUS approximation but in case of using the pointwise approach, spurious velocities appear with no physical meaning.

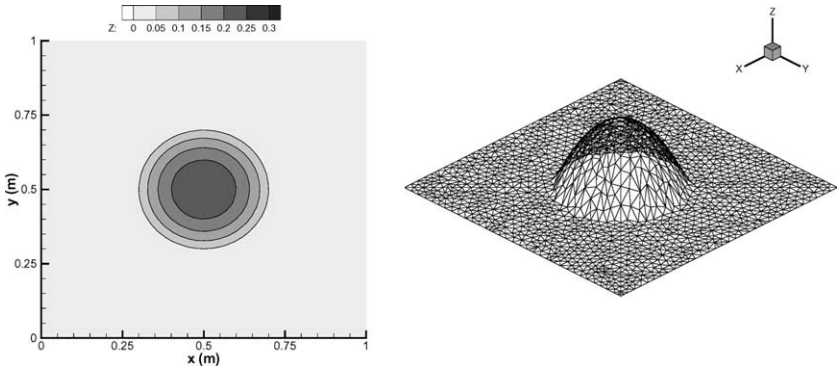

Fig. 4. Geometry of the numerical experiment in terms of iso-contour bottom levels and 3D plot.

In a second situation with initial conditions covering partially the bump,

$$d = h + z_b = 0.1 \text{ m}, \quad u = 0 \text{ m/s}, \quad v = 0 \text{ m/s}, \tag{73}$$

the results are similar. Fig. 6 shows iso-contour levels, velocity field (a,c) and free surface (b,d) after 1 min using the pointwise approach (a,b) for bottom variations or the upwind one (c,d). The wetting–drying condition (70) has been applied in these figures; otherwise water appeared covering the bump. The differences are the same and the use of a MUS discretization for bed slope source terms is totally justified.

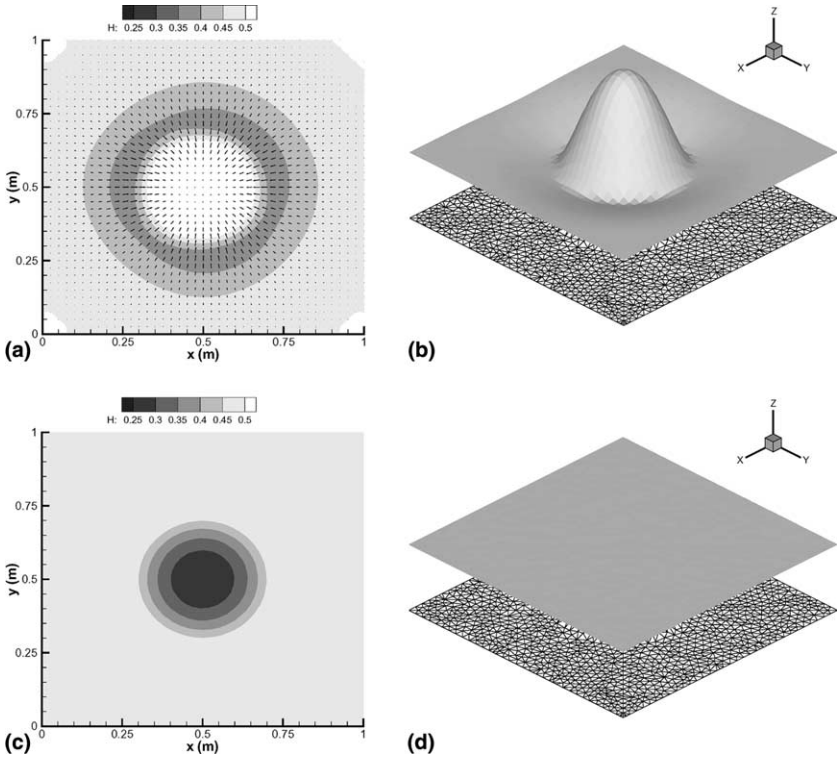

Fig. 5. Comparison of numerical results using a pointwise approach (a,b) or an upwind approach with wetting/drying condition (c,d) in terms of iso-water depth-contours, velocity field (a,c) and free surface (b,d) in case E1 initial conditions are used.

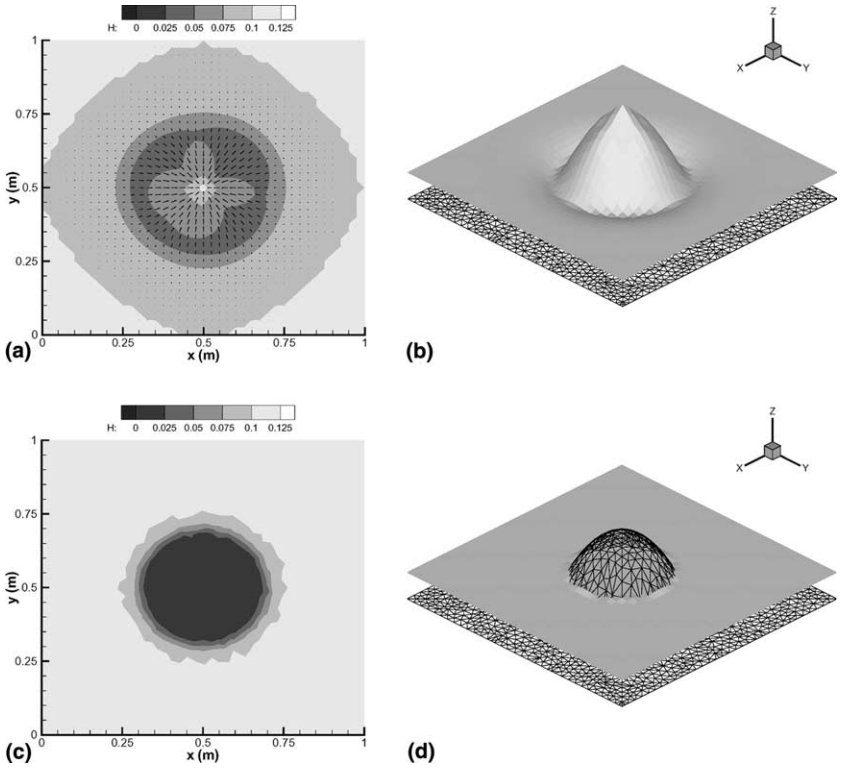

Fig. 6. Comparison of numerical results using a pointwise approach (a,b) or an upwind approach with wetting/drying condition (c,d) in terms of iso-water depth-contours, velocity field (a,c) and free surface (b,d) in case E2 initial conditions are used.

6.2. Dam break through a trapezoidal breach

A two-dimensional flood wave produced by a dam break through a trapezoidal breach is studied. Numerical results obtained by Betcheler et al. [2] in a physical model that represents the propagation of a flood wave are reproduced with the multidimensional upwind technique. The experiment takes place in a reservoir 7 m wide, 2 m long (see Fig. 7) and a flat platform 7 m wide, 5 m long. The dimensions of the trapezoidal breach are specified in Fig. 8. The three boundaries of the platform are open allowing water to go down to another reservoir situated under the platform. The main reservoir is separated from the platform by a wall that contains a breach initially closed. This wall is numerically represented as an elevation of the bottom of the main platform.

Initial conditions are 0.2 m water depth inside the reservoir and dry bed in the rest. Boundary conditions are free outlet and solid walls in the reservoir. Manning's roughness coefficient is $n = 0.01$. Fig. 9 shows time advancing curves of the flood wave at 0.66, 1.02, 1.37, 1.71, 2.08, 2.44 and 2.78 s after the dam break. These results are similar to the experimental ones that can be observed in Fig. 7 of Betcheler et al.'s [2] paper.

It can be observed that after the dam removal, water is symmetrically expanded around the main axis. In Table 1 experimental and numerical results of wetted area during the advancing of the front are compared. In the last column, the numerical error (in %) obtained comparing the wetted area computed with the one measured in each time is included. The values remain below 10%.

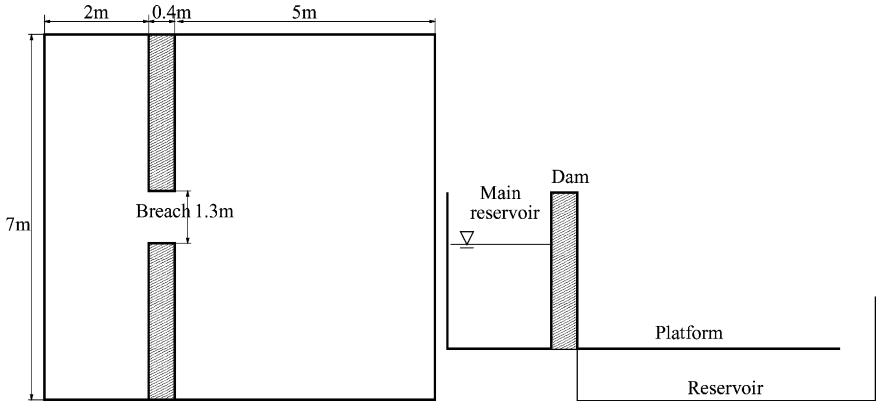

Fig. 7. Physical model of Betcheler's experiment involving the propagation of a flood wave produced by a dam break through a trapezoidal breach.

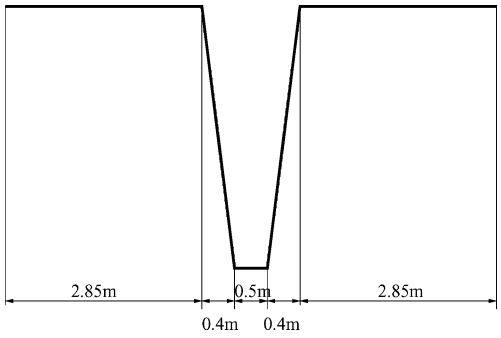

Fig. 8. Details of the trapezoidal breach of the physical model of Betcheler's experiment.

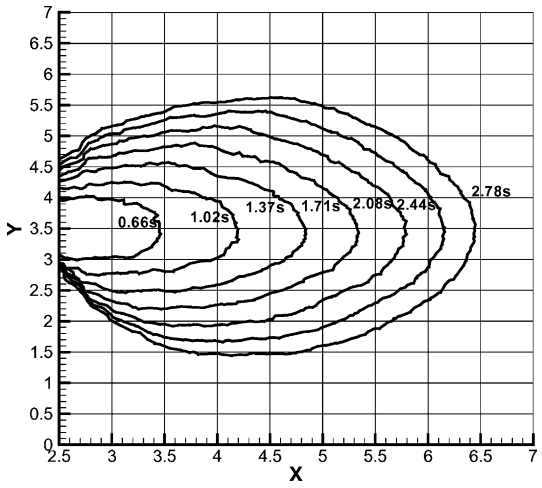

Fig. 9. Time advancing curves of the food wave produced by a dam break through a trapezoidal breach.

Table 1
Experimental and numerical results comparison on the wetted area of the advancing front produced by a dam break through a trapezoidal breach together with mass errors

Time (s)	Wetted area (m^2)		Numerical error (%)
	Experimental	Numerical results	
0.66	0.98	0.94	4.0
1.02	2.10	2.18	3.8
1.37	3.71	3.86	4.0
1.71	5.58	6.18	10.7
2.08	8.25	8.70	5.4
2.44	10.70	11.15	4.2
2.78	13.05	13.52	3.6

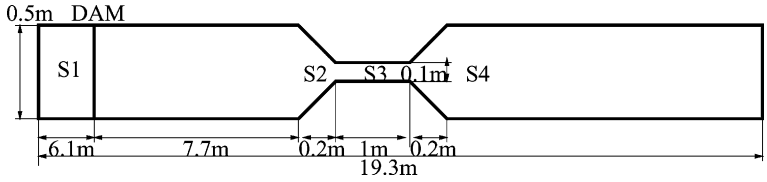

Fig. 10. Geometry of the physical model.

6.3. Dam break in a converging–diverging channel

This test case together with the experimental data was supplied by A. Bento from UTL/IST (Portugal) [1]. A dam break wave propagation through a channel constriction is studied. The advancing front is partially reflected by the walls of the contraction producing a smooth front downstream the channel. Sub- and super-critical flow is produced along the channel. The geometry of the model is detailed in Fig. 10. It consists of a rectangular channel 19.3 m long, 0.5 m wide. The dam is located 6.1 m downstream the first section of the channel. The first constriction section is situated 7.7 m downstream the dam. The constriction is 1 m long and 0.1 m wide and forms 45° with the channel walls. The bottom is flat.

Initial conditions are still water steady state with 0.3 m water depth upstream the dam and 3 mm downstream. Boundary conditions are solid walls except at the outlet that is considered free. Manning coefficient for bottom and walls is $n_b = n_w = 0.01$. The physical domain is discretized in 14207 triangular cells. Fig. 11 shows the comparison between experimental data and numerical results of the water depth time evolution during 10 s at the gauging points. As shown in Fig. 10, S1 is inside the reservoir, S2 is situated before the constriction and we will see the arrival of the dam break front and the reflected front produced in the walls of the constriction. S3 is at the middle of the constriction and there we can only see the arrival of a smoother front and finally S4 is after the constriction in the expanded area and we will see what the front after the constriction looks like. Fig. 12 shows iso-contour water levels (left) and free surface plots (right) at times $T = 5$ (top) and 10 s (bottom).

6.4. Steady and unsteady flows over a channel with three mounds

The physical model presented in this section corresponds to a channel with three mounds located on the channel bottom. The length of the channel is 75 m and its width is 30 m. A plan view and a 3D representation of the channel with its mounds can be seen in Fig. 13. This experimental test is detailed in [19].

In a first simulation, steady state is represented with initially water depth covering totally the small mounds and partially the higher one. Initial flow conditions are

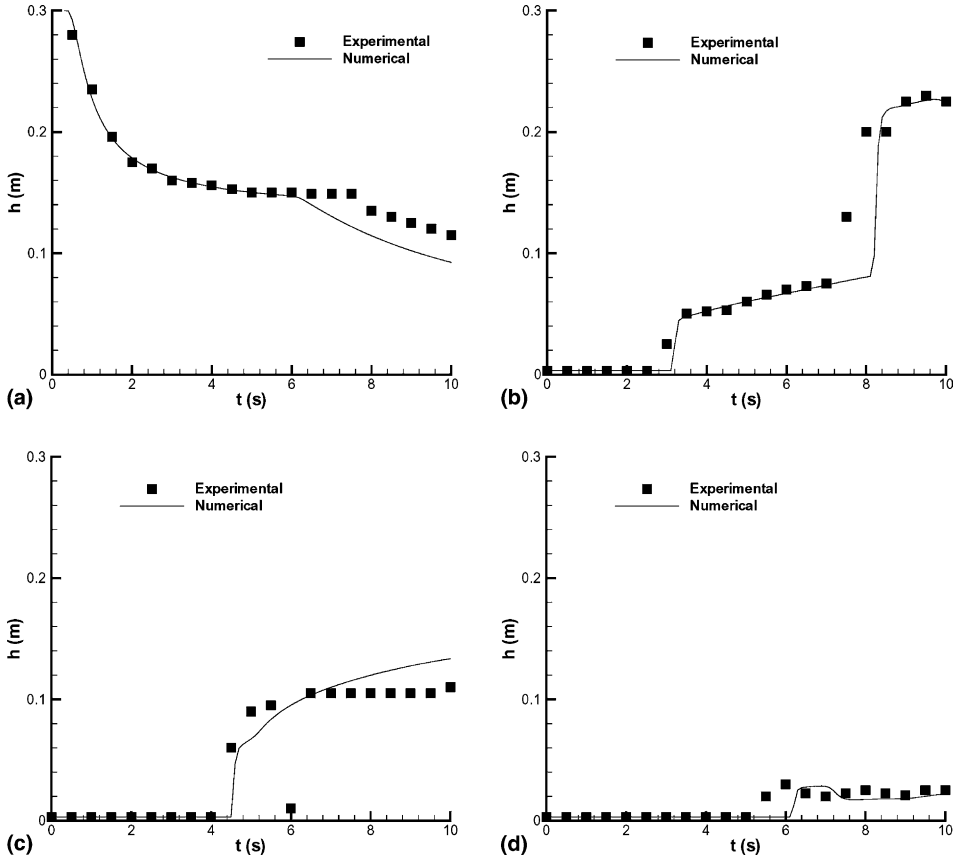

Fig. 11. Comparison between experimental data and numerical results on the time evolution during 10 s of the water depth at the gauging points S1 (a), S2 (b), S3 (c) and S4 (d).

$$d = h + z_b = 0.5 \text{ m}, \quad u = 0 \text{ m/s}, \quad v = 0 \text{ m/s}. \tag{74}$$

Two comparisons are shown in Fig. 14 demonstrating the necessity of applying MUS to the bottom variations source terms and the wetting–drying condition (70) for the wetting front. In that figure, non-physical velocities and water wrong levels can be seen in (a) when a pointwise approach of the bed slope and not wetting–drying condition is used; and the results obtained with the upwind discretization of the bottom variations and the wetting–drying condition which leads to the correct solution are shown in (c), as well as the comparison of free surface levels in (b) and (d). The bottom (mounds) is represented with the grid used in the computation involving 1744 cells, a coarse mesh. It is clearly shown that the pointwise approach of the source terms is not capable of reproducing a high bottom variation and immediately covers all the mounds.

In a second attempt, a dam break flow is analyzed in the same physical model. Initial conditions are $d = h + z_b = 1.875$ m water depth in the first 16 m and dry bed at the rest of the channel. The flood wave evolves and results at time $T = 0$, 15, 25 and 125 s of the dam break front evolution can be seen in Fig. 15. Fig. 16 shows mass error time evolution during 125 s when the wetting/drying condition described in Section 5 is used and when it is not used. The difference between these two approaches generates a 1.5% of mass losses when nothing is done with the wetting fronts over adverse slopes and 0.5% mass gain when the wetting–drying condition (70) is applied.

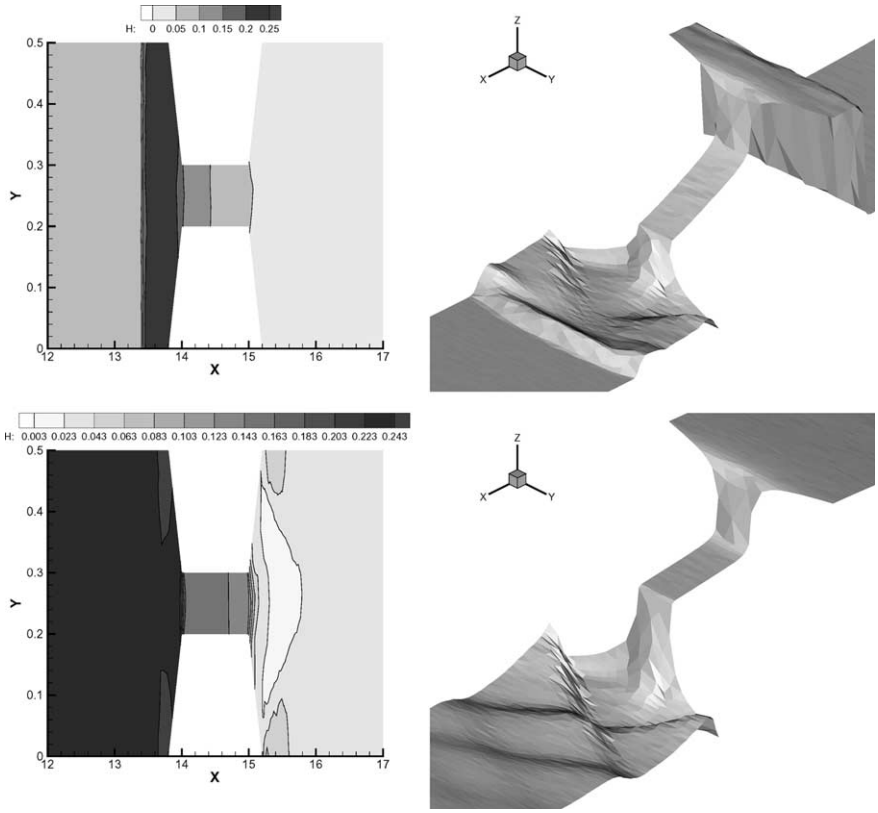

Fig. 12. Iso-contour water levels (left) and free surface plots (right) at times $T = 5$ (top) and 10 s (bottom).

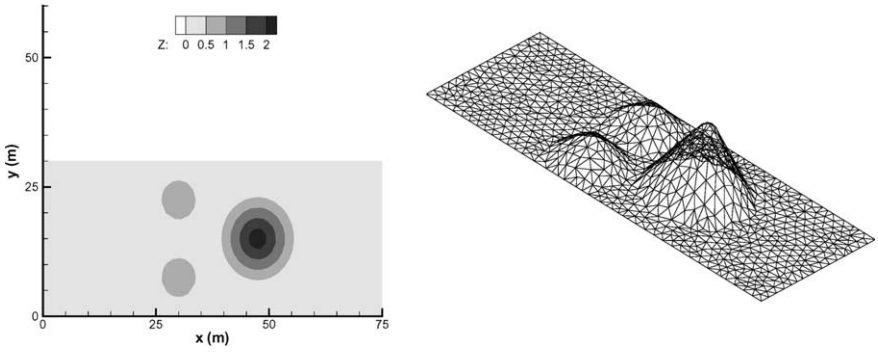

Fig. 13. Plane view and 3D plot of the physical model.

7. Conclusions

A MUS for the solution of the 2D shallow water equations has been applied in first order accuracy for steady and unsteady flows. The basic technique has been extended to cases including variable bed slope. For unsteady flow over variable bed slope the method has been adapted to cope with wetting–drying fronts in a

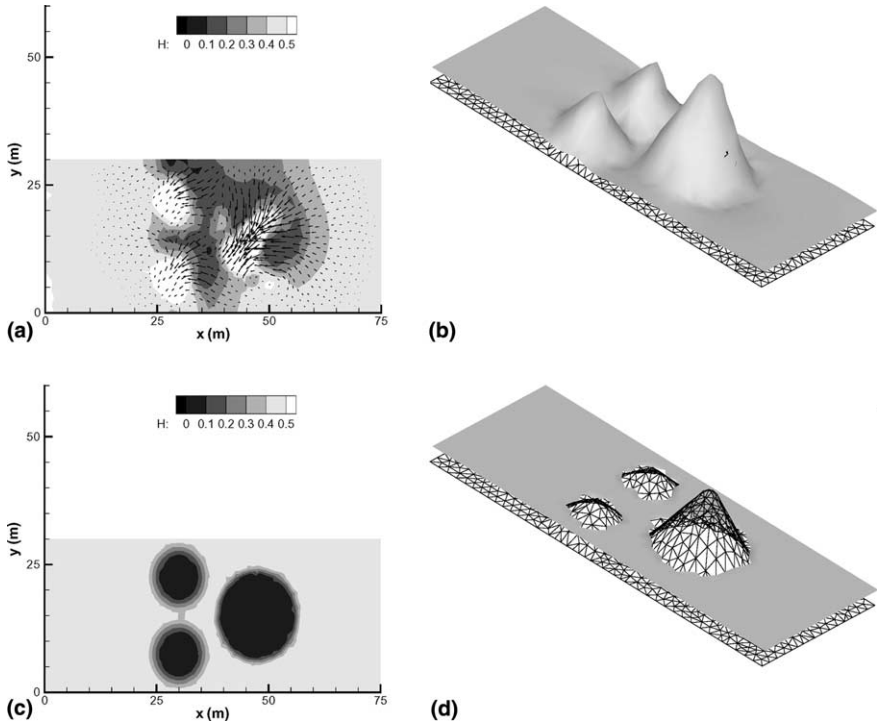

Fig. 14. Comparison of numerical results using a pointwise approach (a,b) or an upwind approach with wetting/drying condition (c,d) in terms of iso-water depth-contours, velocity field (a,c) and free surface (b,d).

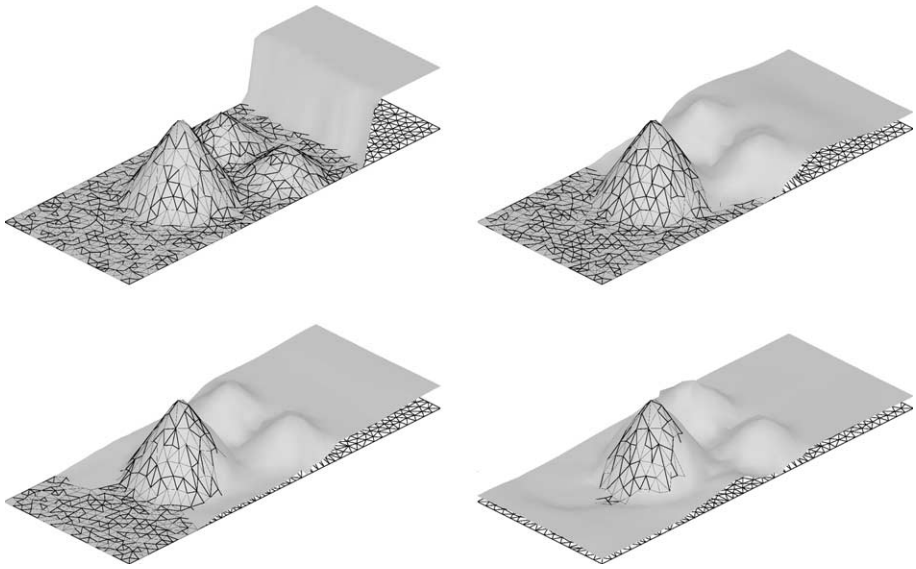

Fig. 15. Free surface plots at times $T = 0$, 15, 25 and 125 s, respectively.

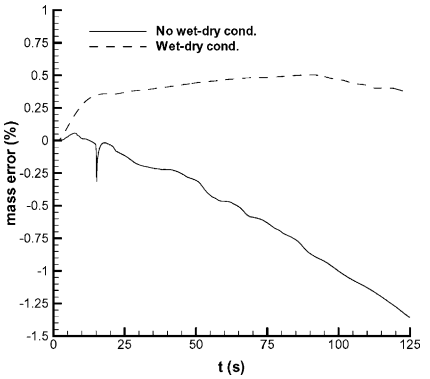

Fig. 16. Mass error time evolution during the computation using or not a special procedure for wetting–drying fronts.

simple and efficient way. The numerical results have been validated by comparison with experimental data in two test cases. The necessity of multidimensional upwinding bottom variations included in the source terms is clearly justified. Mass errors have been controlled during the computation and the multidimensional upwind approach of source terms together with the wetting–drying front treatment obviously reduce them. The multidimensional upwind technique constitutes an alternative promising numerical technique to simulate free surface problems.

References

[1] A. Bento Franco, Modelacao computacional e experimental de escoamentos provocados por roturas de barragens, Ph.D. Thesis, Univ. Técnica de Lisboa, 1996.
[2] W. Betcheler, H. Kulisch, M. Nujic, 2-D dam-break flooding waves comparison between experimental and calculated results, Int. Rep. Inst. of Hydromech and Hyd., Univ. of the Federal Armed Forces, Munich, 1999.
[3] P. Brufau, P. García-Navarro, M.E. Vázquez-Cendón, A numerical model for the flooding and drying of irregular domains, Int. J. Numer. Meth. Fluids 39 (2002) 247–275.
[4] V.T. Chow, Open Channel Hydraulics, MacGraw-Hill, New York, 1959.
[5] S.F. Davis, A rotationally biased upwind difference scheme for the Euler equations, J. Comp. Phys. 56 (1984).
[6] H. Deconinck, C. Hirsch, J. Peuteman, Characteristics decomposition methods for the multidimensional Euler equations, in: 10th Int. Conf. in Num. Met. in Fluid Dyn., 1986, pp. 216–221.
[7] H. Deconinck, R. Struijs, P.L. Roe, Fluctuation splitting for multidimensional convection problem: an alternative to finite volume and finite element methods, in: VKI Lecture series, 1990-03.
[8] H. Deconinck, Analysis of wave propagation properties for the Euler equations in two-space dimensions, in: VKI Lecture series, 1994-05.
[9] H. Deconinck, R. Struijs, G. Bourgois, P.L. Roe, High resolution shock capturing cell vertex advection schemes for unstructured grids, in: VKI Lecture series, 1994-05.
[10] H. Deconinck, B. Koren (Eds.), Euler and Navier–Stokes solvers using multidimensional upwind schemes and multigrid acceleration, Notes on Numerical Fluid Mechanics, vol. 57, Vieweg, 1997.
[11] P. García-Navarro, M.E. Hubbard, A. Priestley, Genuinely multidimensional upwinding for the 2D shallow water equations, J. Comp. Phys. 121 (1) (1995) 79–93.
[12] P. García-Navarro, M.E. Vázquez-Cendón, On numerical treatment of the source terms in the shallow water equations, Comput. Fluids 29 (2000) 951–979.
[13] P. García-Navarro, M.E. Hubbard, P. Brufau, Multidimensional upwind schemes: application to hydraulics, in: Godunov Methods: Theory and Applications, Kluwer Academic Press, 2000.
[14] M. Heniche, Y. Secretan, P. Boudreau, M. Leclerc, A two-dimensional finite element drying-wetting shallow water model for rivers and estuaries, Adv. Water Res. 23 (2000) 359–372.
[15] M.E. Hubbard, Multidimensional upwinding and grid adaptation for conservation laws, Ph.D. Thesis, Univ. of Reading, England, 1996.

[16] M.E. Hubbard, M.J. Baines, Conservative multidimensional upwinding for the steady two-dimensional shallow water equations, J. Comp. Phys. 138 (2) (1997) 419–448.
[17] M.E. Hubbard, P.L. Roe, Compact high-resolution algorithms for time dependent advection on unstructured grids, Int. J. Numer. Methods Fluids (2000).
[18] M.E. Hubbard, P. García-Navarro, Flux difference splitting and the balancing of source terms and flux gradients, J. Comp. Phys. 165 (1) (2000) 89–125.
[19] M. Kawahara, T. Umetsu, Finite element method for moving boundary problems in river flow, Int. J. Numer. Methods Fluids 6 (1986) 365–386.
[20] A.A. Khan, Modelling flow over an initially dry bed, J. Hyd. Res. 38 (5) (2000) 383–389.
[21] R.J. LeVeque, Numerical Methods for Conservation Laws, 2nd ed., Birkhäuser, Basel, 1992.
[22] D. Levy, K.G. Powell, B. Van Leer, Implementation of a grid-independent upwind scheme for the Euler equations, AIAA, 91-0635, 1991.
[23] J. Marz, Improving time accuracy for residual distribution schemes, in: VKI Lecture notes, 1996-17.
[24] H. Paillere, H. Deconinck, E. Van der Weide, Upwind residual distribution methods for compressible flow: an alternative to finite volume and finite element methods, in: VKI Lecture notes, 1997-02.
[25] I.M. Parpia, D.J. Michalek, Grid-independent upwind scheme for multidimensional flow, AIAA J. 31 (4) (1993) 646–651.
[26] P.L. Roe, Discrete models for the numerical analysis of time-dependent multidimensional gas dynamics, J. Comp. Phys. 63 (1986) 458–476.
[27] P.L. Roe, A basis for upwind differencing of the two-dimensional unsteady Euler equations, Numer. Methods Fluid Dyn. II (1986) 55–80.
[28] P.L. Roe, R. Struijs, H. Deconinck, A conservative linearisation of the multidimensional Euler equations, J. Comp. Phys. (1993).
[29] M.A. Rudgyard, Multidimensional wave decompositions for the Euler equations, in: VKI Lecture notes, 1993.
[30] C.L. Rumsey, B. Van Leer, P.L. Roe, A grid-independent approximate Riemann solver with applications to the Euler and Navier–Stokes equations, AIAA (1991) 91–1530.
[31] P.A. Sleigh, M. Berzins, P.H. Gaskell, N.G. Wright, An unstructured finite volume algorithm for predicting flow in rivers and stuaries, Comput. & Fluids (1997).
[32] Y. Tamura, K. Fujii, A multidimensional upwind scheme for the Euler equations on unstructured grids, in: 4th ISCFD Conference, 1991.
[33] E. Van der Weide, Compressible flow simulation on unstructured grids using multi-dimensional upwind schemes, Ph.D. Thesis, Univ. of Delft, The Netherlands, 1998.
[34] M.E. Vázquez-Cendón, Improved treatment of source terms in upwind schemes for the shallow water equations in channels with irregular geometry, J. Comp. Phys. 148 (1999) 497–526.